Electronic Supplementary Information for: CO_2 adsorption on hydroxylated $In_2O_3(110)$

Alvaro Posada-Borbón* and Henrik Grönbeck*

Department of Physics and Competence Centre for Catalysis, Chalmers University of Technology, SE-412 96 Göteborg, Sweden

E-mail: palvaro@chalmers.se,ghj@chalmers.se

Bulk and $In_2O_3(110)$

In_2O_3, is know to exist in nature as three polymorphs with different space group symmetry. Two of these structures are of bcc type, in the bixbyite structure, bixbyite 206 (space group No. 206) and bixbyite 199 (space group No. 199). The third bulk structure, corundum (space group No. 167), is know to exist only at high pressures.[S1,S2] Optimization of the bulk lattice constant is done for the three bulk structures by incremental variation around the experimental lattice constant value. The total system energy per formula unit is plotted in Figure S1, as a function of cell volume. The lattice constant is determined in this way to be l_c = 10.299 Å for bixbyite 206 and l_c = 10.322 Å for bixbyite 199. Corundum, having a rhombohedral symmetry, has lattice vectors $a \neq c$. We find the optimized lattice vectors to be, a = 5.618 Å, c = 14.684 Å. The bulk modulus, B_0, is calculated for each bulk structure by a data fit to an augmented jellium equation of state (SJEOS),[S3] as implemented in the equation of state package in Atomic Simulation Environment (ASE).[S4] The bulk modulus is calculated to be 143, 143 and 192 GPa for bixbyite 206, bixbyite 199 and corundum, respectively.

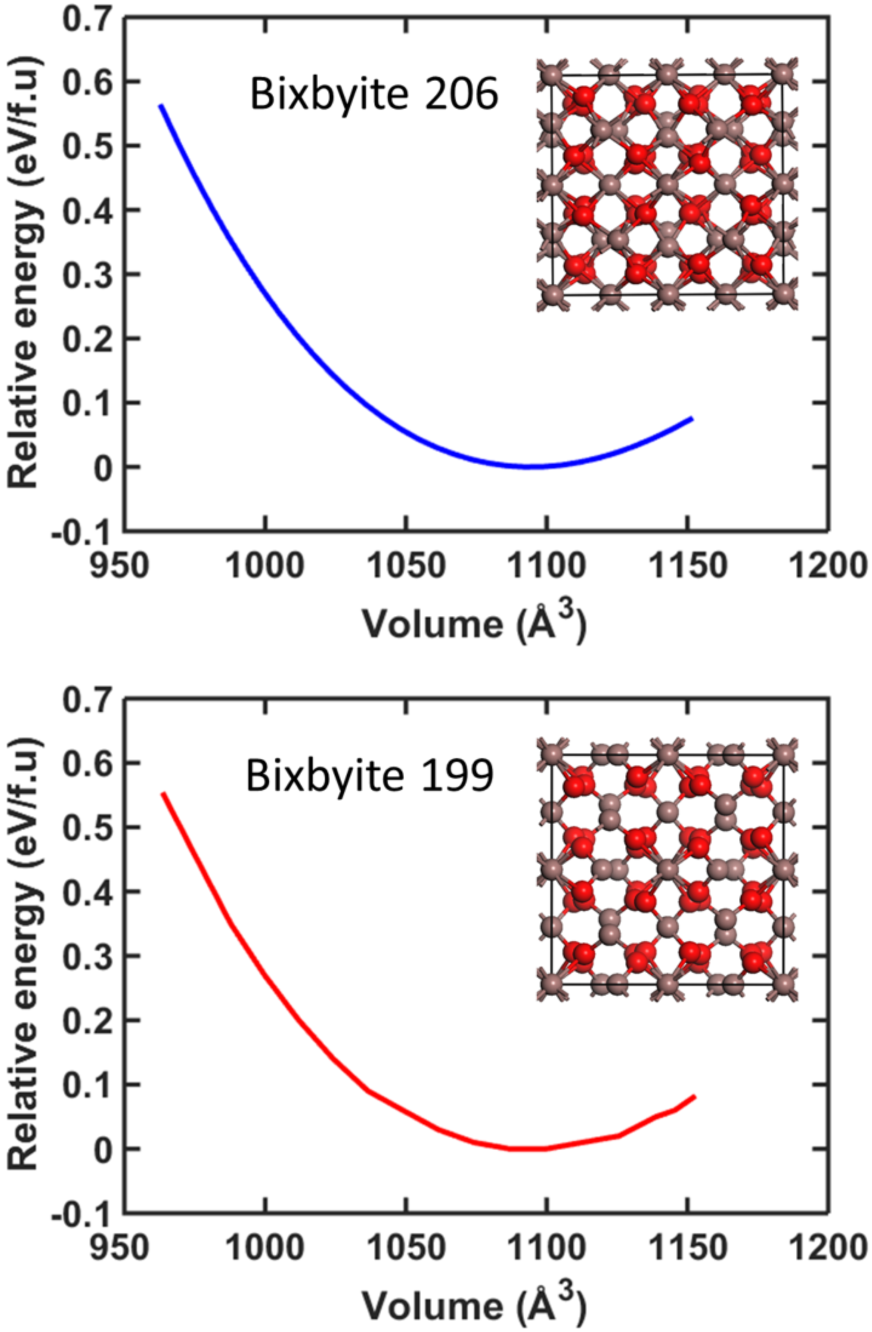

Figure S1: Relative energy of bulk structure per formula unit (f.u.) as a function of cell volume. **Top:** Bixbyite 206. **Bottom:** Bixbyite 199.

Given the similarity between bixbyite 199 and bixbyite 206, the X-ray powder diffraction is simulated for comparison with the experimental observation in.[S5] The simulated XRD calculated with the equilibrium lattice constant is shown in Figure S2.

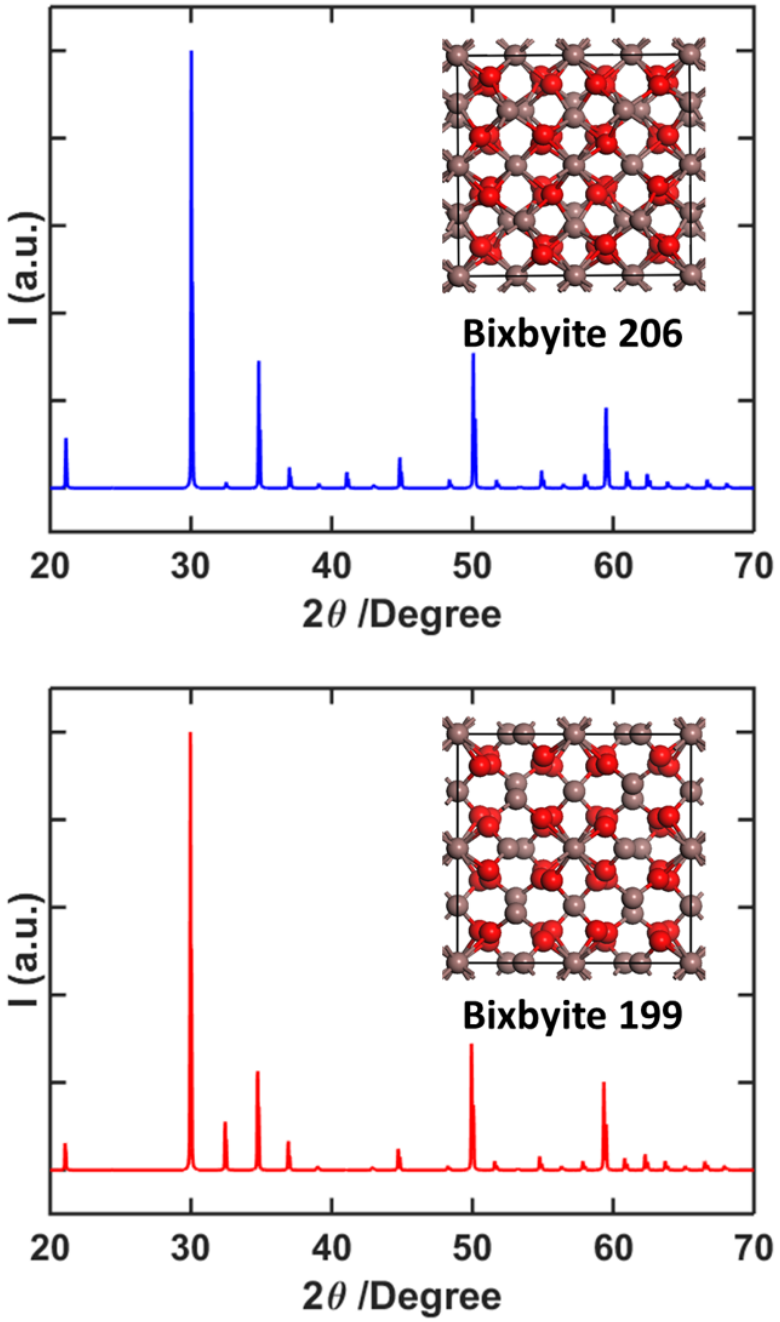

Figure S2: Bulk structure simulated X-ray diffraction pattern. **Top:** Bixbyite 206. **Bottom:** Bixbyite 199.

From the comparison with Ref.,[S5] we notice that the third peak in the spectra for Bixbyite 199, at ∼ 32 °, does not appear in the experimental structure. Moreover, the existence of three peaks at ∼ 37° - 45° on bixbyite 206 shows that this bulk structure is the one observed experimentally.

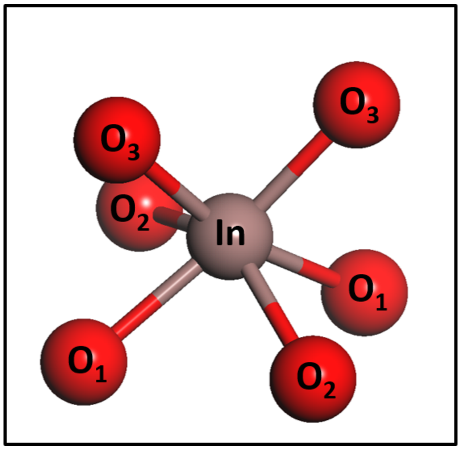

Figure S3: Bixbyite 206 building unit.

As can be observed from Figure S2, the building unit of In_2O_3 is a six-fold oxygen coordinated Indium structure. The detailed morphology of this structure is shown in Figure S3. The interatomic distances are specified in the main text.

H_2 adsorption

Hydrogen average binding energy of all configuration tested on the search of stable structures at different hydrogen coverages are shown in Figure S4. A trend on decreased average binding energy is clearly seen between the lowest lying configuration as hydrogen coverage increases. The spread on hydrogen biding energies reduces as hydrogen coverage increase. Moreover, heterolytic adsorption becomes favorable at a high hydrogen coverage.

We also report here the phase diagram comparison between the adsorption on the 92 % heterolytic site In_4-O_6 and the 83% coverage surface in FigureS5. Where we find that, due to entropic reasons, the 83% hydrogen covered surface is slightly more stable than the heterolytic 92% one. In reaction conditions it is likely then that heterolytically bound hydrogen exists transiently on the surface.

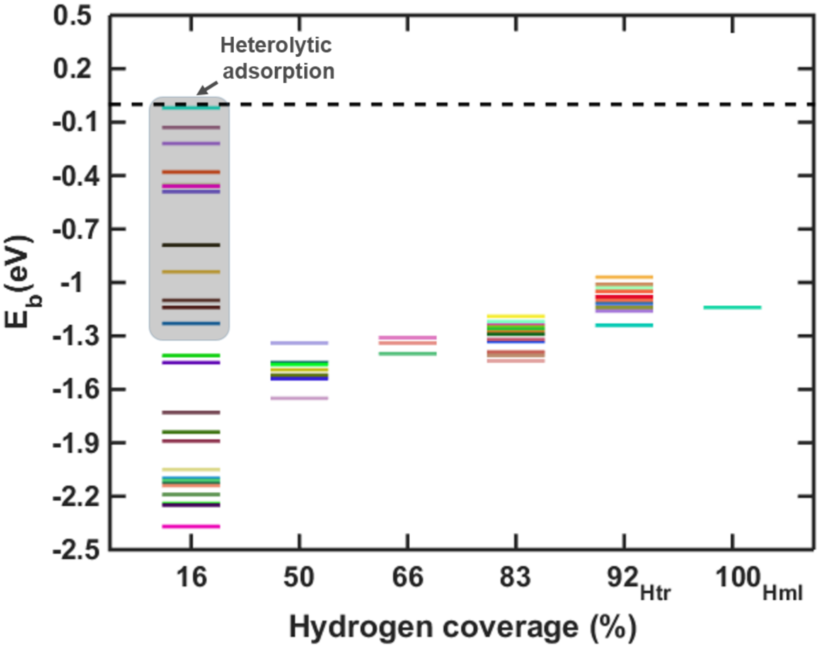

Figure S4: Average hydrogen biding energy as a function of H coverage. All tested sites are presented.

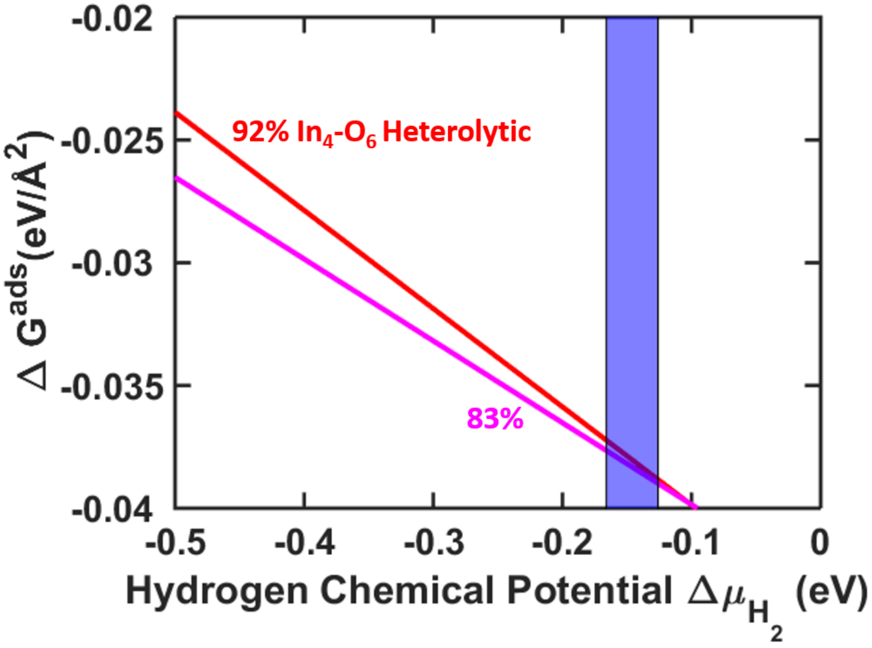

Figure S5: Comparison of surface stability between heterolytic adsorption at 92% coverage and the all-homolytic 83% coverage surface.

H_2O adsorption

Water average binding energy of all configuration tested on the search of stable structures at different hydrogen surface coverages are shown in Figure S6. The top panel in the figure shows the spread of binding energies for the different adsorption modes at the low coverage limit. It is noticeable that the preferred site for molecular adsorption of water is the weakest in comparison with the preferred adsorption sites on all other, dissociated, configurations. The bottom panel of the figure shows the average binding energy on all configurations tested. In this case, we observe a lesser degree on the decrease of water binding energy as the coverage increases. Similarly to hydrogen, the spread in binding energies also decreases significantly with increasing coverage.

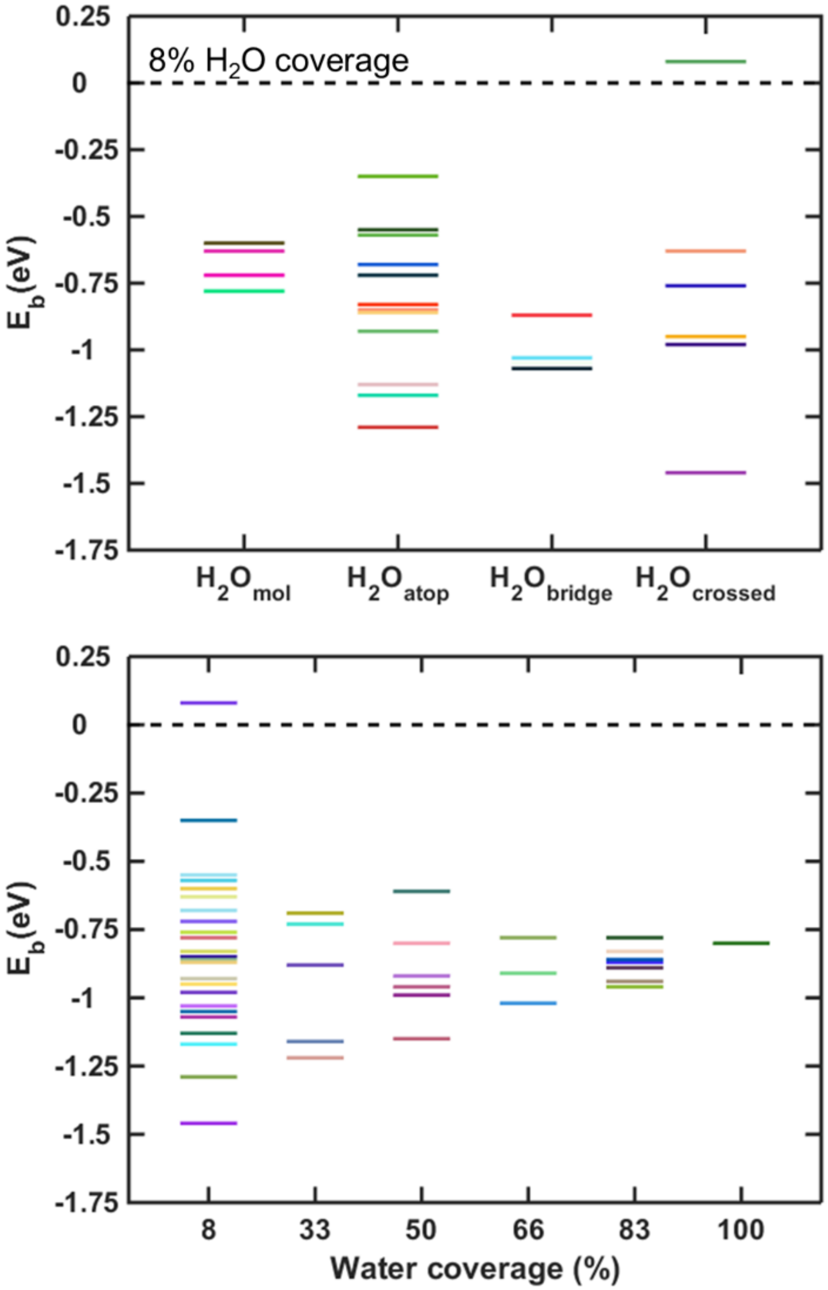

Figure S6: Water average binding energy on $In_2O_3(110)$. **Top.** Adsorption modes at low coverage limit. **Bottom.** Water average binding energy for all configurations tested as a function of coverage.

Oxygen vacancy creation

Several aspects of oxygen vacancy formation are examined in detail to shade light on the effect of hydrogen coverage at methanol synthesis reaction conditions. The oxygen vacancy formation energy is calculated for each oxygen site under different reduction conditions. Namely for thermal desorption, H_2 reduction and CO reduction. The energy is calculated as,

$$E_f(O_v) = (E_{defective} + E_{oxidant}) - (E_{pristine} + E_{reductant}) \tag{1}$$

Where $E_{defective}$ is the energy for the O_v-defective surface, $E_{oxidant}$ is the energy of the product of the different chemical reactions (1/2 E_{O_2}, E_{H_2O} and E_{CO_2}). $E_{pristine}$ is the energy for the defective-free surface and $E_{reductant}$ is the energy of the reducing agent (zero for thermal desorption, E_{H_2} and E_{CO} for the two other cases.) The calculated values for each site are shown in Figure S7

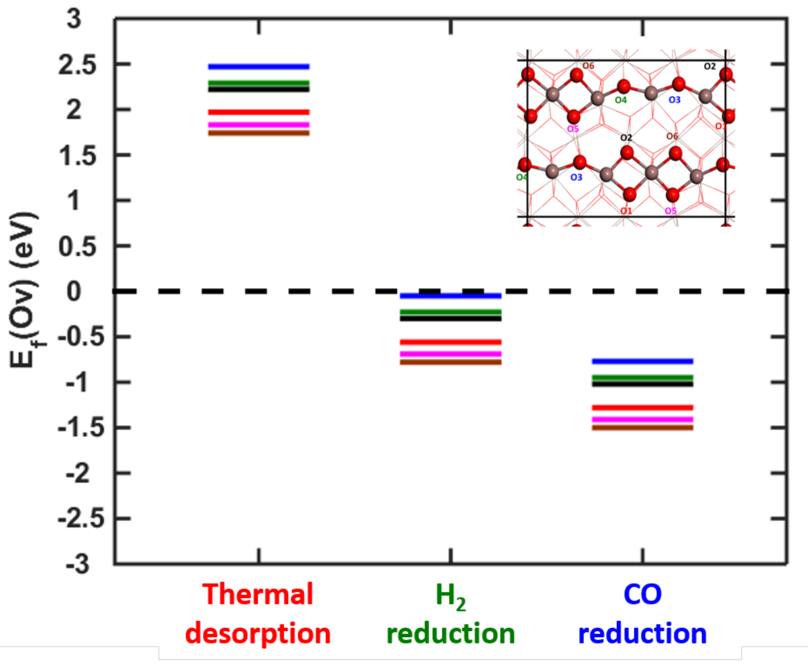

Figure S7: Oxygen vacancy formation energy for each site under different reduction mechanisms.

We find that surface reduction by H_2 and CO is possible for every oxygen site, with CO having a stronger driving force.

We investigated the effect of water partial pressure (P_{H_2O}) and temperature on oxygen vacancy formation by calculating the Gibbs free energy change for the H_2 reduction of site O_2 at hydrogen low coverage limit. See Figure S8 and Figure S9. The O_2 site is selected in our investigation as it exhibits the largest change in Gibbs free energy between the HO_{surf}-HO_{surf} and H_2O(g) state, as shown in Figure 7. Hence, the conditions required to change the favored thermodynamic state of this site are the upper bound to drive the reaction to oxygen vacancy formation at low hydrogen coverage.

To evaluate the pressure effect of water we calculate the Gibbs free energy at 573 K and 3 MPa of H_2 partial pressure. The results are shown in Figure S8.

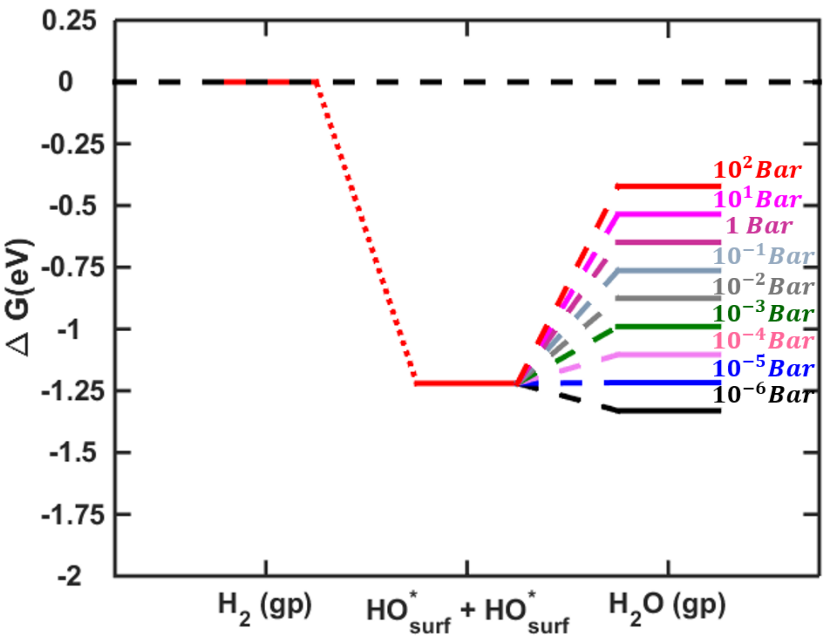

Figure S8: Effect of water partial pressure on oxygen vacancy formation at low hydrogen coverage limit. Gibbs free energy is calculated at 573 K and a hydrogen partial pressure of 3 MPa.

We find that the creation of oxygen vacancies is thermodynamically favorable with respect to H_2(g) even at relatively high water partial pressures. However, the hydroxylated surface becomes unstable once P_{H_2O} is smaller than 10^{-5} Bar, at moderate vacuum conditions.

Reduction of In_2O_3 with H_2 is known to be temperature dependent.[S6] In the same fashion as for the effect of pressure on oxygen vacancy creation, we study the effect of temperature on the Gibbs free energy change for the reduction of the O_2 site. The change in Gibbs free energy is calculated at a water and hydrogen pressure of 1 and 30 bar (0.1 and 3 MPa), respectively. The results are shown in Figure S9

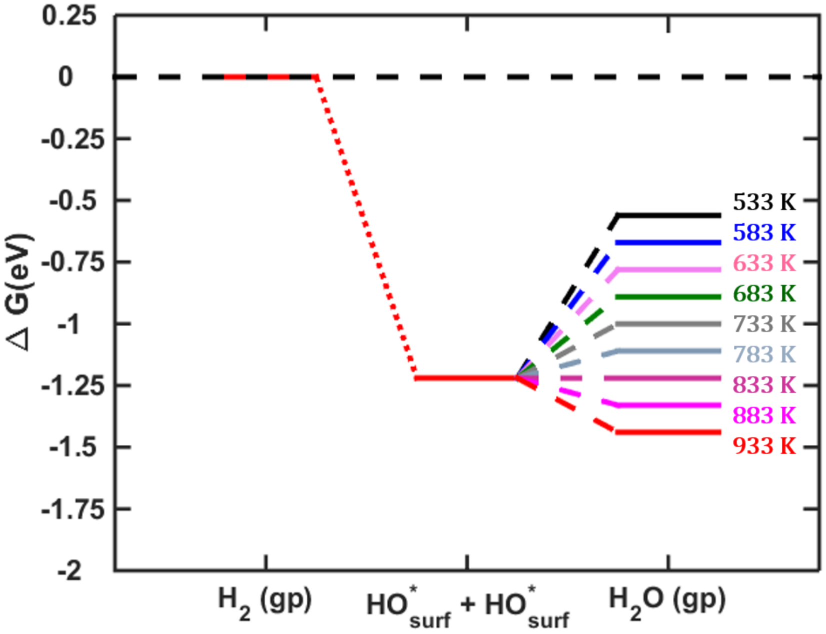

Figure S9: Effect of temperature on oxygen vacancy formation at low hydrogen coverage limit. Gibbs free energy is calculated at partial pressures of 3 and 0.1 MPa for H_2 and H_2O.

We find that increasing temperature can drive oxygen vacancy formation on In_2O_3(110). This result is in accordance to experimental evidence.[S6] However, at low hydrogen coverage conditions temperatures above 833 K are required for this process to be thermodynamically favorable. Our results indicate that oxygen vacancies are only relevant at high hydrogen coverages, as shown in Figure 7 in the manuscript.

The nature of the oxygen vacancies is examined with the use of Bader charge analysis. The charge analysis is done on the most (O_{v6}) and least (O_{v3}) facile oxygen vacancy site found with the energy of vacancy formation analysis. The change in charge is calculated with respect to the pristine surface. Results are reported in Figure S10.

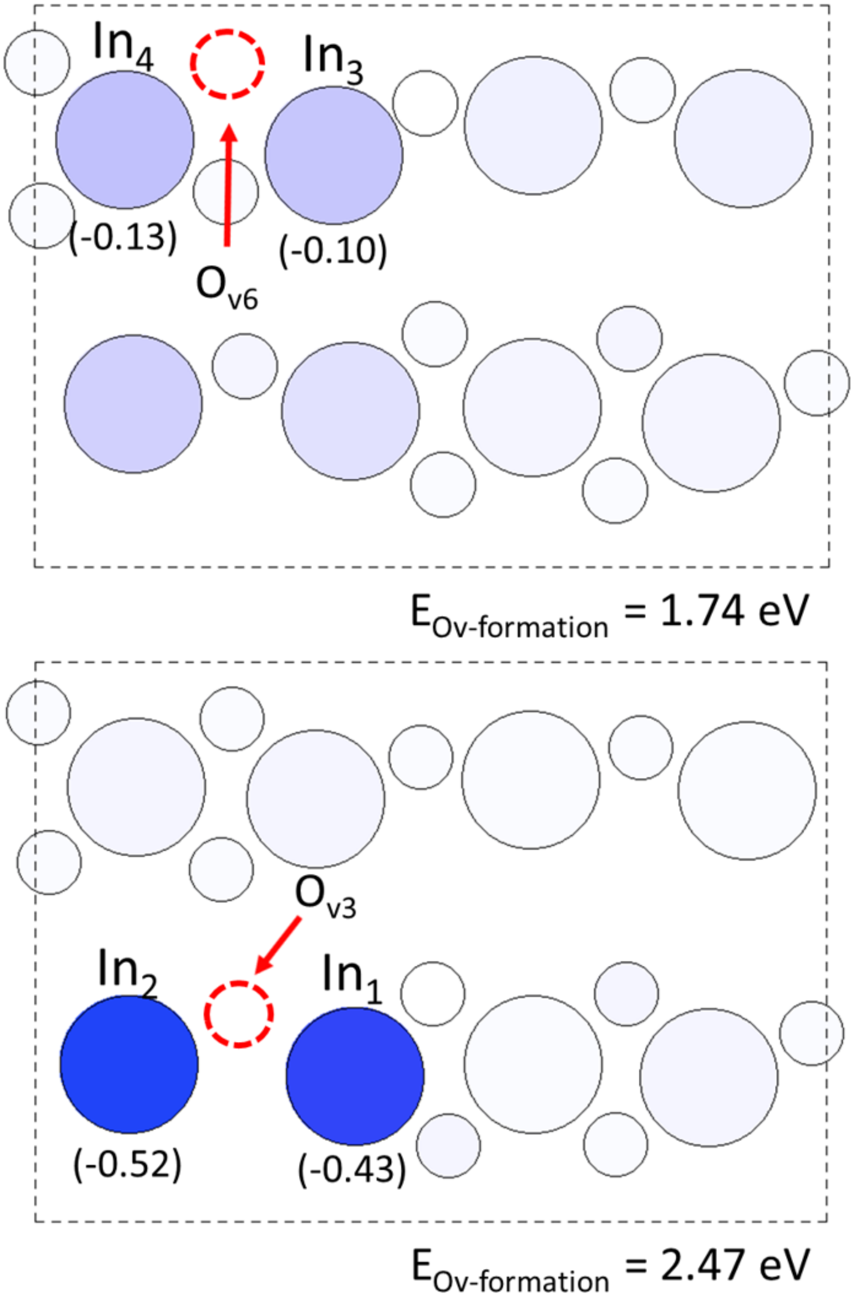

Figure S10: Comparison of nature of oxygen sites by Bader charge analysis on O-defective $In_2O_3(110)$. **Top.** Charge localization on topmost layer atoms around lowest oxygen vacancy formation energy site (O_{v6}). **Bottom.** Charge localization on topmost layer atoms around highest oxygen vacancy formation energy site (O_{v3}). Degree of charge localization is shown in blue.

We find that the oxygen sites are significantly different in nature. For the most facile oxygen vacancy site (O_{v6}), the charge appears to be delocalized all over the surface. With a small charge localization on the neighboring In-sites, In_4 and In_3, of -0.13 and -0.10 e, respectively. In O_{v3}, the oxygen-vacancy site with the highest formation energy, is strikingly different. In this case, the charge is entirely localized on the neighboring In-site, In_1 and In_2 are charged by -0.52 and -0.43 e, respectively, with insignificant charge changes on other atoms. We explain this difference in behaviour as a consequence of the ability of In_1 and In_2 to change oxidation states from +3 to +2. Which is probably linked to the undercoordination of said atoms.

We report here the stability of pairing of oxygen-vacancy sites and unoccupied O-sites that arises when studying the creation of oxygen vacancies at high hydrogen coverage. We report in Figure S11 the oxygen-vacancy formation energy for the all the contiguous O_v-O_{empty} sites at 83 % coverage. For completeness we report the values for the pristine surface.

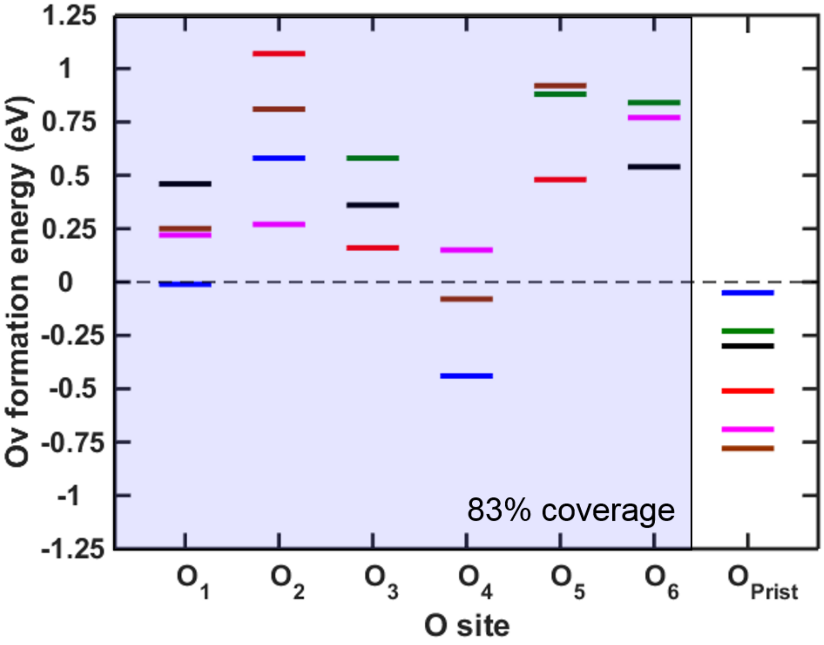

Figure S11: Oxygen vacancy formation energy for each site at 83 %, highlighted in purple, and pristine hydrogen coverages. All possible oxygen pairs are tested on the 83 % coverage sites. Color code as in Figure 1.

Bond valence sum

To analyze the oxidation state of the In-ions, a bond valence sum (BVS) analysis is performed on the pristine and fully H-covered surface (Figure 5 in the main text). The BVS for an In atom in the structure is calculated according to:[S7]

$$BVS = \sum_i exp\left[\frac{(R_0 - R_i)}{b}\right] \tag{2}$$

The sum runs over neighboring atoms, with an interatomic distance cutoff of 2.6 Å. R_0 is calculated to be 1.962 $\AA$ from the average value of the In-O bond-length in the optimized bulk structure, assuming the stoichiometry oxidation state of In (+3). R_i is the interatomic distance between the considered In-atom and the *i-th* oxygen neighbor. b is an empirical constant, which has been determined to be 0.37 $\AA$.[S7] The BVS value for the In-atoms in the bulk is with the determined R_0-value calculated to be 3.01 and 3.05, respectively.

The BVS values for the topmost In-ions in the pristine and H-covered surface with H_2 are given in Table S1. The analysis shows that the oxidation state of the undercoordinated In-atoms is changed to +1 upon H-adsorption, which is consistent with the charge analysis presented in Figure 5 of the main text.

Table S1: BVS-values calculated for In-ions on the top-most layer for the pristine surface and the case with 100 % hydrogen.

Site	BVS (Pristine)	BVS (100 % H-coverage)
In_1	2.62	0.99
In_2	2.65	1.28
In_3	2.69	2.82
In_4	2.71	3.13
In_1-C_2	2.62	0.96
In_2-C_2	2.65	0.99
In_3-C_2	2.69	1.02
In_4-C_2	2.71	3.01

CO_2 adsorption

We report in Table S2 the specific values of all the electronic binding energies of the different cases considered for CO_2 adsorption. Namely, we report adsorption on the six oxygen-vacancy sites on the pristine and hydroxylated surface. We also report the binding energies on all sites tested for the defect-free surface, at pristine, 83 % and 100% hydrogen coverage.

Table S2: Average oxygen binding energy (E_b) calculated for all adsorption modes presented in manuscript.

Site	Coverage (%)	E_b (eV)	Adsorption mode
O_{v1}	Pristine + O_v	—	Physisorbed
O_{v2}	Pristine + O_v	0.29	Fills vacancy
O_{v3}	Pristine + O_v	-0.58	Fills vacancy
O_{v4}	Pristine + O_v	-0.47	Fills vacancy
O_{v5}	Pristine + O_v	—	Physisorbed
O_{v6}	Pristine + O_v	—	Physisorbed
O_1	Pristine	-0.75	Carbonate-like
O_2	Pristine	-0.54	Carbonate-like
O_3	Pristine	-1.37	Carbonate-like
O_4	Pristine	-1.24	Carbonate-like
O_5	Pristine	-0.47	Carbonate-like
O_6	Pristine	-1.21	Carbonate-like
O_{v1}	83 + O_v	-0.48	Goes $CO_2^{\delta-}$
O_{v2}	83 + O_v	0.52	Fills vacancy
O_{v3}	83 + O_v	—	Goes gas phase
O_{v4}	83 + O_v	0.76	Goes $CO_2^{\delta-}$
O_{v5}	83 + O_v	0.20	Goes $CO_2^{\delta-}$
O_{v6}	83 + O_v	0.08	Fills vacancy
In_2In_1	100	-0.71	$CO_2^{\delta-}$
In_1In_2	100	-0.99	$CO_2^{\delta-}$
In_1In_4	100	-0.45	$CO_2^{\delta-}$
In_4In_1	100	—	Physisorbed
In_4In_3	100	—	Physisorbed
In_3In_4	100	—	Physisorbed
In_3In_2	100	-0.51	$CO_2^{\delta-}$
In_2In_3	100	—	Makes water at surface
In_4In_3	83	—	Physisorbed
In_3In_4	83	—	Physisorbed
O_5	83	-0.08	Carbonate-like

We find that adsorption in the oxygen vacancies is less favored than adsorption on the defect-free surface, at all hydrogen coverages.

References

(S1) de Boer, T.; Bekheet, M. F.; Gurlo, A.; Riedel, R.; Moewes, A. Band gap and electronic structure of cubic, rhombohedral, and orthorhombic In_2O_3 polymorphs: Experiment and theory. *Phys. Rev. B* **2016**, *93*, 1552051–1552057.

(S2) Karazhanov, S. Z.; Ravindran, P.; Vajeeston, P.; Ulyashin, A.; Finstad, T. G.; Fjellvag, H. Phase stability, electronic structure, and optical properties of indium oxide polytypes. *Phys. Rev. B* **2007**, *76*, 0751291–07512913.

(S3) Alchagirov, A.; Perdew, J.; Boettger, J.; Albers, R.; Fiolhais, C. Energy and pressure versus volume: Equations of state motivated by the stabilized jellium model - Reply. *Phys. Rev. B* **2003**, *67*.

(S4) Bahn, S.; Jacobsen, K. An object-oriented scripting interface to a legacy electronic structure code. *Comput. Sci. Eng.* **2002**, *4*, 56–66.

(S5) Martin, O.; Martin, A. J.; Mondelli, C.; Mitchell, S.; Segawa, T. F.; Hauert, R.; Drouilly, C.; Curulla-Ferre, D.; Perez-Ramirez, J. Indium oxide as a superior catalyst for methanol synthesis by CO_2 hydrogenation. *Angew. Chem. Int. Ed.* **2016**, *55*, 6261–6265.

(S6) Bielz, T.; Lorenz, H.; Jochum, W.; Kaindl, R.; Klauser, F.; Kloetzer, B.; Penner, S. Hydrogen on In_2O_3: reducibility, bonding, defect formation, and reactivity. *J. Phys. Chem. C* **2010**, *114*, 9022–9029.

(S7) Brown, I. D. Recent Developments in the Methods and Applications of the Bond Valence Model. *Chem. Rev.* **2009**, *109*, 6858–6919.